technologies

MDPI

Article

Design of a Bidirectional Veneer Defect Repair Method Based on Parametric Modeling and Multi-Objective Optimization

Xingchen Ding [1,2], Jiuqing Liu [2], Xin Sun [1,2], Hao Chang [1,2], Jie Yan [1,2], Chengwen Sun [2,*] and Chunmei Yang [1,2,*]

[1] Forestry and Woodworking Machinery Engineering Technology Center, Northeast Forestry University, Harbin 150006, China; reicl@nefu.edu.cn (X.D.); 15142177527@163.com (X.S.); m18955813458@163.com (H.C.); yanjie1690@163.com (J.Y.)
[2] College of Mechanical and Electrical Engineering, Northeast Forestry University, Harbin 150006, China; nefujdljq@163.com
* Correspondence: sunchengwen@nefu.edu.cn (C.S.); ycmnefu@126.com (C.Y.)

Abstract

Repairing veneer defects is the key to ensuring the quality of plywood. In order to improve the maintenance quality and material utilization efficiency during the maintenance process, this paper proposes a bidirectional maintenance method based on gear rack transmission and its related equipment. Based on the working principle, a geometric relationship model was established, which combines the structural parameters of the mold, punch, and gear system. Simultaneously, it solves the problem of motion attitude analysis of conjugate tooth profiles under non-standard meshing conditions, aiming to establish a constraint relationship between stamping motion and structural design parameters. On this basis, a constrained optimization model was developed by integrating multi-objective optimization theory to maximize maintenance efficiency. The NSGA-III algorithm is used to solve the model and obtain the Pareto front solution set. Subsequently, three optimal parameter configurations were selected for simulation analysis and experimental platform construction. The simulation and experimental results indicate that the veneer repair time ranges from 0.6 to 1.8 seconds, depending on the stamping speed. A reduction of 28 mm in die height decreases the repair time by approximately 0.1 seconds, resulting in an efficiency improvement of about 14%. The experimental results confirm the effectiveness of the proposed method in repairing veneer defects. Vibration measurements further verify the system's stable operation under parametric modeling and optimization design. The main vibration response occurs during the meshing and disengagement phases between the gear and rack.

Keywords: parametric modeling; multi-objective optimization; meshing motion; veneer defect repair; vibration response

check for updates

Academic Editor: Simone Genovesi

Received: 2 July 2025
Revised: 27 July 2025
Accepted: 29 July 2025
Published: 31 July 2025

Citation: Ding, X.; Liu, J.; Sun, X.; Chang, H.; Yan, J.; Sun, C.; Yang, C. Design of a Bidirectional Veneer Defect Repair Method Based on Parametric Modeling and Multi-Objective Optimization. *Technologies* **2025**, *13*, 324. https://doi.org/10.3390/technologies13080324

Copyright: © 2025 by the authors. Licensee MDPI, Basel, Switzerland. This article is an open access article distributed under the terms and conditions of the Creative Commons Attribution (CC BY) license (https://creativecommons.org/licenses/by/4.0/).

1. Introduction

Veneer serves as a primary base material in plywood manufacturing, which is produced by stacking multiple layers in orthogonal orientations and bonding them together using resin-based adhesives [1]. This manufacturing process is not only simple but also highly reliable. Compared to solid wood panels, the resulting plywood demonstrates superior dimensional stability and mechanical strength, while offering a wider range of size options and greater flexibility in application [2]. Consequently, this material has found extensive use across various industries, including construction, furniture manufacturing, and interior decoration [3].

After rotary cutting, veneer surfaces commonly exhibit defects such as knots, cracks, and decay. These imperfections are primarily attributed to natural factors during tree growth, as well as technical errors that occur during the processing stages [4,5]. The presence of such defects not only compromises the surface appearance but also adversely affects the mechanical properties of the veneer. If left unaddressed, these flaws may propagate into cracks during subsequent manufacturing processes, thereby increasing the likelihood of board cracking, warping, and poor bonding performance [6].

In plywood production, one of the most critical objectives is to maximize both the yield and quality of the veneer [7]. Therefore, the effective use area of veneer must be guaranteed as much as possible in the production process. For the defects on a single board, the common repair method is to use the defect-free plate cutting to make a patch to replace the defect area [8]. This localized repair approach effectively increases the overall utilization area of the veneer. The selected patch wood is matched to the original veneer in both material composition and grain texture, ensuring visual and structural consistency of the repaired surface.

In the field of defect repair technology, Kauranen et al. [9] from Raute Corporation proposed a repair process based on a dual-punch system. The first set of punches is used to precisely remove the defective area, while the second set is responsible for forming the patch and pressing it into the excised region. Patterson et al. [10] proposed the use of thermosetting resin as a base material to prepare a synthetic compound for filling veneer defects. However, this method faces challenges in achieving uniform control over the material composition during practical implementation, which may lead to inconsistent repair performance. Metz [11] further proposed a method combining a patch insertion adjustment device with milling machining, offering improved accuracy in the repair process. Despite its precision advantages, this technique is not well suited for repairing thin veneer sheets, limiting its applicability in certain manufacturing contexts.

The removal of defective areas and the fabrication of repair patches primarily rely on stamping motion. Therefore, the rational design of the stamping stroke and related component dimensions plays a crucial role in improving repair efficiency [12]. Xie et al. [12] conducted a detailed analysis of pressure distribution during the stamping process and employed an improved optimization algorithm to adjust key parameters such as stamping force and blank holder travel, resulting in significantly enhanced component quality. Awasthi et al. [13] further emphasized the significance of the stamping stroke, identifying it as one of the most critical factors influencing the forming process. Meanwhile, Kuo et al. [14] demonstrated that forming time could be reduced by 0.06 seconds through optimization of the pulsation curve in servo press operations.

Meanwhile, in the optimization research of mechanical systems, integrating mathematical modeling with optimization algorithms has proven to be a crucial approach for enhancing system performance. Okotete [15] successfully applied the NSGA-III-based multi-objective optimization framework to obtain Pareto-optimal solutions for the primary suspension stiffness and steering linkage parameters of a forced-steering passenger train, establishing a systematic methodology for parameter optimization in complex mechanical systems. Davoodi et al. [16,17] developed predictive models for the load-bearing capacity of NiP/TiN duplex coatings on 6061 aluminum alloy using partial least squares (PLS) and support vector regression (SVR), with coating thickness, adhesion strength, and elastic modulus as key input variables. Additionally, response surface methodology (RSM) was employed to investigate the tribological behavior under dry sliding conditions, identifying the critical design parameters that significantly influence coating performance. Zhai et al. [18] established a mathematical model of the conveying capacity and motion equations for the telescopic rod end, revealing the relationship between the rotation center position

and structural parameters, and further identifying evaluation metrics and key influencing factors for conveying performance. In conclusion, mathematical modeling provides a solid theoretical foundation for performance analysis in mechanical systems, while optimization algorithms effectively enhance multi-dimensional performance indicators without compromising operational requirements.

Currently, research on veneer defect repair has predominantly focused on functional implementation. The operational workflow still contains a degree of design redundancy, and a systematic analysis of the correlation between key mechanical parameters and the kinematic and dynamic characteristics of the mechanism remains lacking. The rack-and-pinion mechanism offers a compact structure, making it well-suited for mold design. Its reciprocating motion characteristic also helps eliminate redundant steps in traditional repair methods, thereby improving the overall efficiency of the system. This study proposes a reciprocating punch design based on a rack-and-pinion mechanism, aiming to enable efficient bidirectional repair of veneer defects. By analyzing the deformation behavior of the veneer under compressive stress and the kinematic characteristics during the stamping process, parametric models of both the punch and die are developed. These models are then incorporated into a multi-objective optimization framework. The NSGA-III algorithm will be employed to determine the optimal combination of structural parameters, with the objective of enhancing repair efficiency and improving system operational stability.

2. Repair Methodology and Structural Design

2.1. Repair Methodology

This study proposes an improved repair strategy based on the method introduced by Kauranen et al. [9], as illustrated in Figure 1. The proposed strategy optimizes stamping time intervals and integrates the offcuts of the patch base blank with the waste generated from defect removal. This combined material can be utilized for the production of low-end products or for the preparation of biomass pellets [19]. This approach effectively prevents resource wastage that would otherwise occur if large quantities of defect-generated materials and patch blank scraps were disposed of in landfills [20], while also enabling efficient and automated ejection of waste from the system.

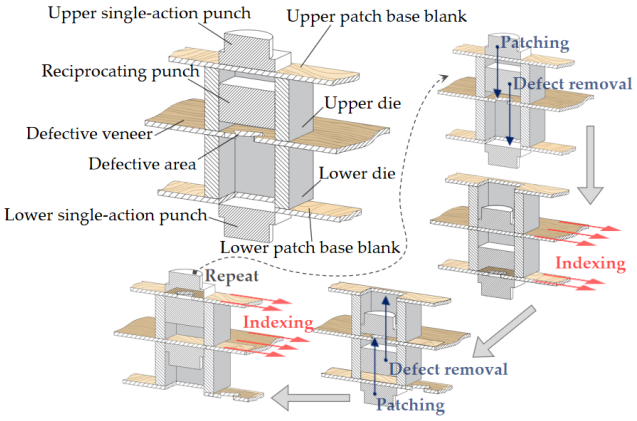


Figure 1. Schematic diagram of the defect repair methodology.

The improved repair method proposed in this study consists of five main components:

(1) Single-action punches (divided into upper and lower sets): These are used to stamp out patches from the patch base blank for repairing defect areas.
(2) Dies (divided into upper and lower sets): These work in conjunction with the punches to achieve shearing and blanking of the veneer sheets.

(3) Patch base blanks (divided into upper and lower sets): These serve as the base material for creating patches.
(4) Reciprocating punch: This component is responsible for removing defect areas by cutting and pressing the generated waste into the excision site.
(5) Defective veneers: These are the target objects for repair.

The unidirectional punch and the reciprocating punch operate in synchronized motion in the same direction, allowing simultaneous blanking of both the defective veneer and the patch base blank. Consequently, defect removal and patch formation are nearly completed at the same time. This design not only enables rapid repair of the defective area but also synchronously compresses the generated waste into the holes formed in the patch base blank during cutting. Compared to the method proposed by Kauranen et al., the present approach optimizes the operational sequence, thereby enhancing both repair efficiency and resource utilization.

2.2. Structural Design

The single-action punch is typically actuated by a pneumatic or hydraulic cylinder, while the veneer sheet is positioned and transported using a conveyor system or vacuum suction device. The key innovation of the proposed method lies in the design of the reciprocating punch, which enables rapid bidirectional movement within the upper and lower dies, thereby achieving efficient removal of defective areas on the veneer sheet.

This study designs a mechanical system based on the rack-and-pinion meshing principle, as illustrated in Figure 2. The main components include a slotted die and a partial tooth gear, which engages only partially with the rack. The gear is designed with an involute tooth profile. The reciprocating punch consists of a mounting plate, a rack, an upper cutting blade, and a lower cutting blade. Notably, both blades are configured with the same tooth profile as the rack, ensuring synchronized motion and precise meshing performance.

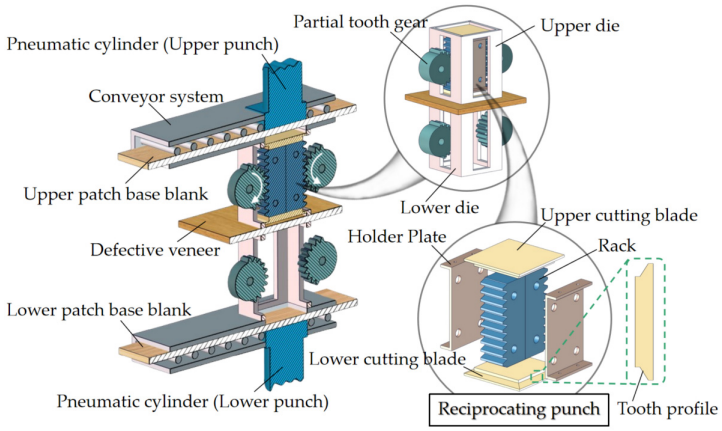


Figure 2. Structural composition of the repair system.

Two sets of gear systems are arranged above and below, allowing the reciprocating punch to be transferred between two die regions through the engagement of one set of gears. Upon reaching the second die region, the reciprocating punch engages with the second set of gears. Due to the partial tooth design of the gears, the previous set automatically disengages once the new engagement begins, thereby enabling controlled reciprocating motion of the punch between the two die areas. Furthermore, the stamping process of the single-action punch within the dies does not interfere with the gear mechanisms.

3. Modeling and Optimization Design of the Stamping Process

3.1. Parametric Modeling and Constraint Analysis of the Reciprocating Punch Motion Process

3.1.1. Constraint Analysis Between Veneer Thickness and Blade Thickness

After the punching and blanking process, the defective scrap tends to approximately adhere to the surface of the blade, forming a structure similar to a rack gear. This can subsequently affect the meshing behavior between the blade and the driving gear.

As illustrated in Figure 3, the operating conditions can be categorized into two scenarios based on the scrap thickness h and the punch blade thickness s_p. When the sum of these two parameters exceeds the tooth tip thickness of the rack gear s_a, i.e., $h + s_p > s_a$, an interference region arises during the meshing process of the subsequent pair of teeth. The extent of this interference is characterized by the interference height Δs. Such a condition should be avoided as much as possible, as the meshing interference can significantly increase contact wear between the gear and the rack, and may also cause damage to the fiber structure at the edge of the veneer.

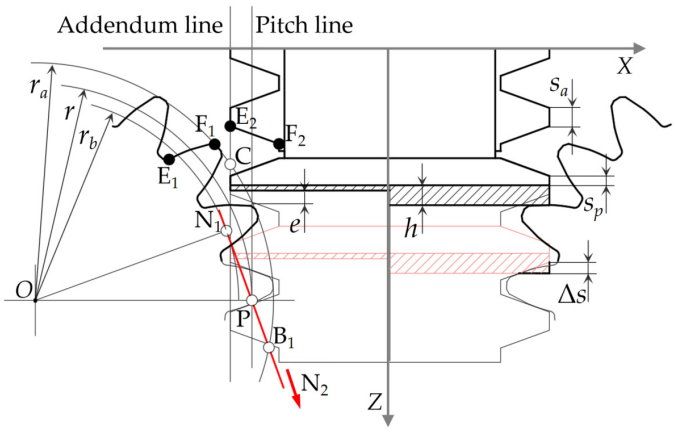


Figure 3. Meshing relationship after veneer blanking.

When the sum of the two is less than the rack crest thickness s_a, i.e., $h + s_p < s_a$, the actual mesh contact point is offset by a distance e in the Z direction compared to the standard rack and pinion mesh, resulting in an early contact between the gear profile $\widehat{E_1E_2}$ and the rack profile $\widehat{F_1F_2}$ in the next pair of teeth. When the offset distance e exceeds the maximum contact distance of the next pair of teeth before entering engagement (i.e., the maximum distance CF_1 between the intersection of tooth profile $\widehat{E_1E_2}$ and tooth profile $\widehat{F_1F_2}$ and the tooth crest line), there will be no effective contact point between tooth profile $\widehat{E_1E_2}$ and tooth profile $\widehat{F_1F_2}$, resulting in gear tooth misalignment during engagement. When the offset distance e is less than CF_1, there is an effective contact point between the tooth profile $\widehat{E_1E_2}$ and the tooth profile $\widehat{F_1F_2}$. In this condition, the original meshing zone develops a certain amount of backlash due to the offset e. As the tooth profiles $\widehat{E_1E_2}$ and $\widehat{F_1F_2}$ come into contact and bear the load, the presence of backlash leads to an increase in angular acceleration, which causes the gear tooth to deflect toward the backlash region. This process can be regarded as a self-correcting behavior during gear meshing, after which the subsequent teeth enter into normal engagement.

The offset e and the distance CF_1 can be derived based on the geometric relationships during gear meshing, as illustrated in Figure 4. In Figure 4a, assuming that the meshing point of a pair of conjugate tooth profiles at the moment of disengagement is B_1, the distance CF_1 can be calculated as the difference between F_1B_1 and CB_1. Specifically, CB_1 represents the displacement of point B_1 along the Z direction as it rotates to point C, while F_1B_1 is determined based on the displacement of the rack.

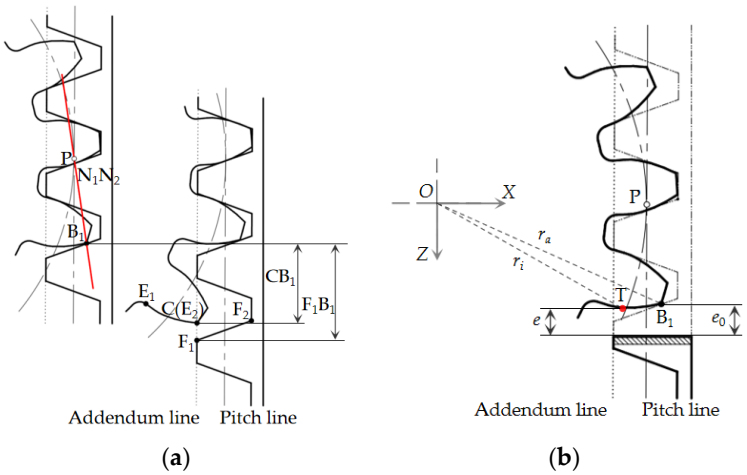


Figure 4. Geometric constraints of CF_1 and e: (**a**) geometric definition of CF_1 during gear meshing, (**b**) geometric definition of e during gear meshing.

The coordinates of point B_1 are expressed as (B_1^X, B_1^Z), and those of point C are expressed as (C^X, C^Z). With the origin of the coordinate system located at the gear center O, the distance CB_1 can be calculated as the absolute difference between the Z-coordinates of the two points, i.e., $CB_1 = |C^Z - B_1^Z|$. The coordinates of point B_1 can be determined based on the projections of the segment PB_1 along the X and Z directions, where PB_1 lies on the line of action N_1N_2. The line of action N_1N_2 is determined based on the pitch point P and the gear base circle radius r_b (see Figure 3).

$$\begin{cases} B_1^X = r\sin a\cos\alpha(\tan\alpha_a - \tan\alpha') + r \\ B_1^Z = -r\cos^2\alpha(\tan\alpha_a - \tan\alpha') \end{cases} \tag{1}$$

The coordinates of point C are determined using the chord length formula:

$$\begin{cases} C^X = r - h_a^* m \\ C^Z = -\sqrt{r_a^2 - (r - h_a^* m)^2} \end{cases} \tag{2}$$

The distance F_1B_1 consists of two components: first, the rack displacement corresponding to the rotation of the gear from point B_1 to point C; and second, the vertical (Z-directional) spacing between the meshing point B_1 and the rack tooth tip F_1 along the tooth profile. The corresponding mathematical expression is given by Equation (3):

$$F_1B_1 = \frac{2\pi r}{180}\arcsin\left[\frac{\sqrt{(B_1^X - C^X)^2 + (CB_1)^2}}{2r_a}\right] + r\sin^2\alpha(\tan\alpha_a - \tan\alpha') + h_a^* m\tan\alpha \tag{3}$$

By combining Equations (1)–(3), the relational equation for CF_1 can be obtained, which is expressed in terms of structural parameters as follows:

$$\begin{aligned} CF_1 = {} & h_a^* m\tan\alpha - 2\sqrt{rmh_a^*} + r(\tan\alpha_a - \tan\alpha') \\ & + \frac{2\pi r}{180}\arcsin\left(\frac{\sqrt{[(4rmh_a^*)^{0.5} - r\cos^2\alpha(\tan\alpha_a - \tan\alpha')]^2 + [h_a^* m + r\sin\alpha\cos\alpha(\tan\alpha_a - \tan\alpha')]^2}}{2r_a}\right) \end{aligned} \tag{4}$$

The structural parameters included in the equation are the module m, the addendum coefficient h_a^*, the gear pitch circle radius r, the gear tip circle radius r_a, the tip pressure angle α_a, and the meshing angle α'. Under standard installation conditions, the meshing angle α' is equal to the pressure angle α of the dividing circle, which is 20°. Additionally, the addendum coefficient is set to $h_a^* = 1$.

Figure 4b illustrates the geometric relationship of the offset e during the meshing process. Let point T be a point on the involute tooth profile, which is also the tangent point between the tooth profile and the horizontal line and is located on the circle with radius r_i. The coordinates of point T are expressed as (T^X, T^Z). The offset distance e can be further decomposed into the distance from the disengaging point B_1 to the board surface (recorded as e_0) minus the maximum distance difference between the point B_1 and the tangent point T in the Z direction, i.e., max ($\left|T^Z\right| - \left|B_1^Z\right|$), where e_0 can be calculated based on the coordinates of point B_1, as given by Equation (5):

$$e_0 = [r \sin a \cos a(\tan \alpha_a - \tan \alpha') - h_a^* m] \times \tan \alpha + \frac{1}{2}\pi m - s_p - h \tag{5}$$

As shown in Figure 4b, during the disengagement phase, points T and B_1 can be considered to lie on the same involute tooth profile. Consequently, the coordinates of point T can be expressed in terms of those of point B_1 using a rotation matrix.

$$\begin{cases} T^X = \frac{r_i}{r_a}(B_1^X \cos \angle TOB_1 - B_1^Z \sin \angle TOB_1) \\ T^Z = \frac{r_i}{r_a}(B_1^Z \cos \angle TOB_1 + B_1^X \sin \angle TOB_1) \end{cases} \tag{6}$$

The angle $\angle TOB_1$ denotes the central angle corresponding to points T and B_1, which is determined by calculating the arc tooth thickness along the circle of radius r_i, as expressed in Equation (7). In the equation, "inv" denotes the involute function [21], and α_i is the pressure angle at point T on the involute.

$$\angle TOB_1 = -\frac{180}{\pi}(\text{inv}\alpha_a - \text{inv}\alpha_i) \tag{7}$$

Combining Equations (5)–(7), the relationship equation about e is obtained, which is expressed as follows by structural parameters:

$$\begin{aligned} e = e_0 - \max(T^Z - B_1^Z) &= [r \sin a \cos a(\tan \alpha_a - \tan \alpha') - h_a^* m] \times \tan \alpha + \tfrac{1}{2}\pi m - s_p - h \\ &-\max\{r \cos^2 \alpha(\tan \alpha_a - \tan \alpha') \tfrac{r_i \cos[\frac{180}{\pi}(\text{inv}\alpha_a - \text{inv}\alpha_i)] - r - h_a^* m}{r + h_a^* m} \\ &+ \tfrac{r r_i}{r + h_a^* m}[\sin a \cos \alpha(\tan \alpha_a - \tan \alpha') + 1] \sin[\tfrac{180}{\pi}(\text{inv}\alpha_a - \text{inv}\alpha_i)]\} \quad r_i \in [\max(r - 1.25m, r_b), r_a] \end{aligned} \tag{8}$$

3.1.2. Stamping Motion and Structural Parameter Constraint Analysis

The reciprocating punch must perform two key operations within its stamping stroke: first, to complete the blanking of the veneer defect, and second, to press the resulting waste into the hole in the trimmings. The realization of this functionality depends on two critical aspects of motion control. First, the reciprocating punch must be able to smoothly transition from one gear system to another. Second, the angular displacement of the gear system must provide sufficient stroke support to ensure completion of the entire stamping cycle.

According to the design requirements for continuous transmission [22], the total contact ratio of the two gears during meshing should be no less than 1 to ensure continuous and stable power transmission. The ideal scenario is that the upper and lower gears achieve fully synchronized motion. As shown in Figure 5, when the upper gear disengages at point B_1, one flank of the lower gear also disengages synchronously at point B_3, while the other flank begins to engage at point B_2. At this moment, the distance between the stamping surface of the reciprocating punch and the bottom surface of the upper die is denoted as H_{R1}. This distance serves as a critical condition for ensuring stable meshing and enabling a smooth transition of the reciprocating punch. In addition, after the lower gear comes into contact with the reciprocating punch at point B_2, it must drive the punch to continue its downward movement until reaching the bottom of the lower die. This

stroke is denoted as H_{R2}. To ensure the complete execution of the stamping motion, the displacement stroke generated by a single gear driving the reciprocating punch must be sufficient to satisfy both H_{R1} and H_{R2}. This relationship can be expressed in terms of the gear's angular displacement θ (°), as follows:

$$\frac{\theta r \pi}{180} > \begin{cases} H_{R1} = \frac{1}{2}[a + s_b + \frac{r}{2}\cos^2\alpha(\tan\alpha_a - \tan\alpha')] + s_p + 2h_a^* m\tan\alpha \\ H_{R2} = l_{ud} - \frac{a-s_b}{2} + h_a^* m\cot\alpha + h \end{cases} \quad (9)$$

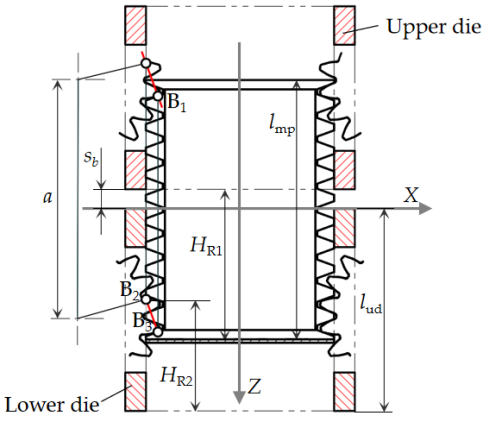


Figure 5. Positional relationship of the upper and lower gears.

In the equation, s_b represents the distance between the upper and lower dies. During the punching and shearing process of the defect, the defective veneer is clamped and fixed by the upper die, at which point the distance s_b equals the veneer thickness h. The parameter a denotes the center distance between the upper and lower gears. By connecting the line segment between the meshing points B_1 and B_3, it can be observed that the center distance corresponds to the total pitch length on the rack with a tooth count of z_R, i.e., $a = \pi m z_R$. l_{ud} denotes the total height of the die, which must accommodate the full height of the reciprocating punch. Extra space should also be reserved for the impact distance to increase both kinetic and potential energy, thus enhancing stamping performance. Let l_{mp} be the height of the reciprocating punch; the geometric constraint between the punch and the die is given by the following expression:

$$l_{ud} > l_{mp} = a + 2s_p + 0.5m\pi + 2h_a^* m\tan\alpha \quad (10)$$

In addition, the total height l_{ud} of the die should also be greater than the diameter r_a of the tooth tip circle of the gear to avoid interference between the gear and the defective veneer during operation.

The gear structure used in this paper is not a standard structure with complete circumferential teeth, but a limited number of effective teeth are arranged in local areas to participate in the actual meshing. This design prevents structural interference that could occur during the stamping stroke of the single-action punch after the gear has driven the reciprocating punch.

In this design, the meshing zone determines both the range of the gear's angular displacement θ and the number of teeth z_G that are actually involved in meshing. This tooth count can be calculated using the ceil function (rounding up to the nearest integer).

$$z_G = \mathrm{ceil}(\frac{\theta r}{180m}) \quad (11)$$

The non-meshing zone occupies the remaining angular range (i.e., $360 - \theta$), and its profile is formed by a cylindrical surface with a radius smaller than that of the gear root

circle. This cylindrical radius is defined as r_0, as shown in Figure 6. Define points A_3 and A_4 as the two intersection points between the inner wall of the slot and the gear's tip circle diameter. The arc segment corresponding to the cylindrical surface should not intersect with the line segment A_3A_4, and the arc region must be greater than the central angle $\angle A_3OA_4$. The central angle $\angle A_3OA_4$ can be expressed in terms of lengths using the law of cosines:

$$360 - \theta \geq \angle A_3OA_4 = \arccos[1 - \frac{1}{2} \times (\frac{A_3A_4}{r_a})^2] \quad (12)$$

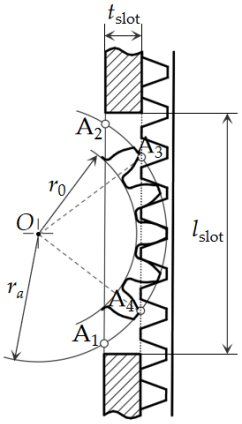


Figure 6. Constraint relationship between the gear tip circle diameter and the die slot.

The length of the line segment A_3A_4 can be obtained using the chord length formula:

$$A_3A_4 = 2\sqrt{(2h_a^*m + \delta)(2r_a - 2h_a^*m - \delta)} \quad (13)$$

where δ represents the blanking clearance, which has a significant influence on the quality of the shear edge of the veneer [23]. The smoothness of the sheared surface and the presence of burrs directly affect the effectiveness of the subsequent repair process. An excessively small punch–die clearance increases the contact stress on the punch, which, under long-term operation, accelerates the degradation of tool accuracy and the accumulation of surface damage [24,25]. In contrast, an overly large clearance tends to result in pronounced burr formation and elevated surface roughness on the shear edge [26]. In the field of die design, empirical formulas are commonly employed to estimate the appropriate clearance value [27]. Reichel [28] reported that a suitable punch–die clearance should be maintained between 5% and 12% of the veneer thickness, depending on material properties and process requirements.

Additionally, the positioning layout of the gears imposes requirements on the die thickness. As shown in Figure 6, the upper and lower gears engage with the rack through slots cut into the sides of the die. If the slot height l_{slot} and the die thickness t_{slot} are not properly designed, they can also affect the meshing motion of the gears.

Assuming the gear center is located on the central plane of the slot, the slot height l_{slot} can be approximately expressed using the ceil and floor functions (rounding up and down to the nearest integer, respectively), based on the geometric relationships shown in Figures 5 and 6, as illustrated in Equation (14).

$$l_{slot} \approx \text{ceil}[a - h - 2 \times \text{floor}(\frac{a - h - A_1A_2}{2})] \quad (14)$$

Points A_1 and A_2 are the intersection points between the outer wall of the slot and the gear's tip circle diameter. The length of the line segment A_1A_2 must be less than the slot height l_{slot}, which can be calculated using the chord length formula, as shown in

Equation (15). The die thickness t_{slot} in the equation can be determined based on empirical formulas from relevant mold design handbooks [29,30]. For blanking thin sheet materials, it should be selected to be greater than 25 mm.

$$\mathrm{A_1A_2} = 2\sqrt{r_a^2 - [r - (mh_a^* + \delta + t_{\text{slot}})]^2} \tag{15}$$

3.2. Multi-Objective Optimization

Based on the above analysis, all constraint conditions required to realize the stamping motion and its associated geometric structure have been obtained. These constraints are denoted as g_i and presented in Equation (16). Among them, a total of seven design variables are involved in the optimization process: the gear module m, the rack tooth number z_{R}, the gear pitch radius r, the cylindrical surface radius r_0, the punch blade thickness s_p, the total height of the die l_{ud}, and the gear angular displacement θ. All other parameters involved are known constants or predefined input conditions.

$$\begin{cases} g_1 = \frac{2r}{m} - 17 \geq 0 \\ g_2 = h + s_p - s_a < 0 \\ g_3 = \frac{1}{2}[a + h + \frac{r}{2}\cos^2\alpha(\tan\alpha_a - \tan\alpha')] + s_p + 2h_a^* m\tan\alpha - \frac{\theta r\pi}{180} < 0 \\ g_4 = l_{\text{ud}} - \frac{a - s_b}{2} + h_a^* m\cot\alpha + h - \frac{\theta r\pi}{180} < 0 \\ g_5 = l_{\text{mp}} - l_{\text{ud}} < 0 \\ g_6 = l_{\text{ud}} - 2(r + mh_a^*) > 0 \\ g_7 = h + 2(r + mh_a^*) - a < 0 \\ g_8 = r - 1.25m - r_0 > 0 \\ g_9 = r - mh_a^* - \delta - r_0 > 0 \\ g_{10} = l_{slot} - \mathrm{A_1A_2} > 0 \\ g_{11} = 360 - \theta - \angle\mathrm{A_3OA_4} \geq 0 \\ g_{12} = e - \mathrm{CF_1} < 0 \end{cases} \tag{16}$$

During the optimization design process, it is also necessary to set upper and lower bounds for the design variables to define the search space [31]. For example, the gear module m and the pitch radius r determine the overall size of the gear, which indirectly affects the stamping stroke. Therefore, they should not be designed to be excessively large. The upper limit of the module m is set to 10, and the upper limit of the pitch radius r is set to 100 mm. The number of rack teeth z_{R} should be no less than five to ensure effective meshing; at the same time, to avoid increasing unnecessary stroke distance, its value should not be excessively large. The punch blade thickness s_p is limited by the tooth tip thickness of the rack and can be estimated based on the gear module m. The specific upper and lower bounds are defined as follows.

$$\Omega = \begin{cases} 1 \leq m \leq 10 \\ 5 \leq z_{\text{R}} \leq 20 \\ 8.5 \leq r \leq 100 \\ 6 \leq r_0 \leq 100 \\ 1 \leq s_p \leq 10 \\ 40 \leq l_{\text{ud}} \leq 250 \\ 20 \leq \theta \leq 360 \end{cases} \tag{17}$$

In the parameter optimization process, in addition to meeting the basic functional requirements, improving repair efficiency is also a key design objective. To this end, the optimization model should be constructed with the objective of minimizing the following performance indicators: the number of gear teeth z_{G} actually involved in meshing, the height l_{mp} of the reciprocating punch, the gear center distance a, and the driving displace-

ment of the gear on the reciprocating punch. The minimization of these parameters helps to reduce the stamping stroke, thereby improving repair efficiency. In addition, the die should be designed to reasonably accommodate the reciprocating punch, avoiding structural redundancy caused by excessive dimensions. Based on the above considerations, the following multi-objective optimization function is established:

$$\min f = (z_G, \frac{\theta r \pi}{180}, l_{mp}, l_{ud} - l_{mp}, a) \tag{18}$$

3.3. Multi-Objective Optimization Algorithm

The NSGA-III algorithm is an improved multi-objective evolutionary algorithm developed based on the NSGA-II framework. Its core enhancement lies in the introduction of a reference point selection mechanism [32]. When dealing with optimization problems involving two or more objectives, the NSGA-III algorithm can effectively improve convergence speed and population diversity, thereby avoiding common issues such as uneven distribution of the solution set and getting trapped in local optima [33,34]. As mentioned earlier, the optimization model established in this study involves five objective functions and exhibits typical characteristics of a high-dimensional multi-objective problem. The NSGA-III algorithm is therefore adopted to address this challenge. The flowchart of the algorithm is shown in Figure 7.

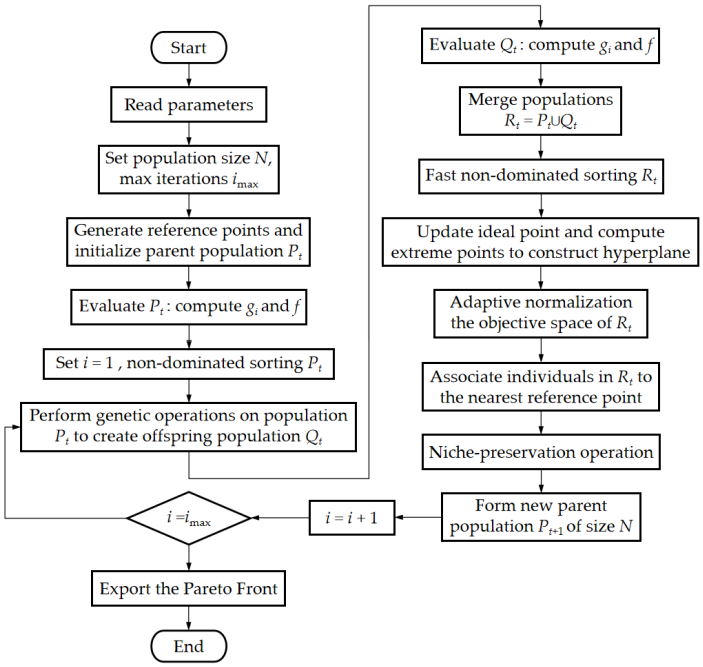


Figure 7. Flowchart of the NSGA-III algorithm.

4. Case Study and Validation

4.1. Optimization Solution

Taking poplar veneer as an example, the material was sourced from the Dasan Plate Processing Plant in Yanshou County, Heilongjiang Province, China. The measured thickness of the veneer is h = 1.5 mm, which was incorporated as an input parameter into the optimization model.

The optimization process was carried out using the PlatEMO toolbox, an open-source platform developed in MATLAB R2020b for solving complex optimization problems [35]. In the optimization setup, the population size was set to 1000, and the number of iterations was set to 10,000. Based on the principle of minimizing the gear-driven displacement of the

reciprocating punch as well as the heights of both the punch and die, a total of 15 optimal feasible solutions were selected, as shown in Table 1.

Table 1. Optimized parameter dataset.

No.	Design Variables							Objective Function				
	m	z_R	r (mm)	r_0 (mm)	s_p (mm)	l_{ud} (mm)	θ (°)	z_G	$\theta r\pi/180$ (mm)	l_{mp} (mm)	$l_{ud} - l_{mp}$ (mm)	a (mm)
1	3	7	25.50	21	1.02	104	201.63	10	89.74	74.91	29.09	65.97
2	3	7	28.50	21	1.01	128	219.92	12	109.39	74.90	53.10	65.97
3	5	7	47.50	38	2.46	127	107.26	6	88.92	126.37	0.63	109.96
4	4	8	40	27	1.49	137	147.01	9	102.63	112.70	24.30	100.53
5	5	7	47.50	39	1.75	133	117.25	7	97.20	124.95	8.05	109.96
6	3	11	25.50	20	1.00	122	246.62	12	109.76	112.57	9.43	103.67
7	4	9	42	27	1.46	140	150.01	9	109.96	125.22	14.78	113.10
8	5	7	45	38	2.50	155	159.35	8	125.15	126.45	28.55	109.96
9	4	11	52	28	1.28	159	115.24	9	104.59	149.98	9.02	138.23
10	6	7	54	46	2.20	156	130.52	7	123.01	150.14	5.86	131.95
11	5	8	45	29	2.66	157	173.42	9	136.20	142.48	14.52	125.66
12	6	7	51	38	2.55	173	147.66	7	131.44	150.85	22.15	131.95
13	4	10	54	34	1.43	144	153.68	12	144.84	137.71	6.29	125.66
14	7	7	66.50	50	2.83	182	109.65	6	127.27	175.70	6.30	153.94
15	8	7	68	56	4.06	211	134.87	7	160.06	202.43	8.57	175.93

	Constraints											
	g1	g2	g3	g4	g5	g6	g7	g8	g9	g10	g11	g12
1	0	−0.01	−51.22	−8.23	−29.09	−47	−7.47	−0.75	−1.35	−2.25	−81.66	−0.73
2	−2	−0.01	−70.85	−3.89	−53.10	−65	−1.47	−3.75	−4.35	−2.00	−67.25	−0.76
3	−2	−0.25	−24.41	−0.91	−0.63	−22	−3.46	−3.25	−4.35	−1.90	−180.29	−1.03
4	−3	−0.39	−45.06	−2.65	−24.30	−49	−11.03	−8.00	−8.85	−2.72	−142.12	−0.67
5	−2	−0.97	−33.41	−3.19	−8.05	−28	−3.46	−2.25	−3.35	−1.90	−170.29	−0.32
6	0	−0.03	−52.41	−29.10	−9.42	−65	−45.17	−1.75	−2.35	−2.25	−36.68	−0.71
7	−4	−0.41	−46.11	−13.27	−14.78	−48	−19.60	−10.00	−10.85	−1.66	−140.73	−0.67
8	−1	−0.21	−60.63	−9.14	−28.54	−55	−8.46	−0.75	−1.85	−1.51	−126.34	−1.04
9	−9	−0.59	−28.29	−1.47	−9.02	−47	−24.73	−19.00	−19.85	−0.75	−182.16	−0.61
10	−1	−1.36	−46.54	−14.25	−5.86	−36	−10.45	−0.50	−1.85	−2.04	−155.26	−0.15
11	−1	−0.05	−63.67	−26.05	−14.52	−57	−24.16	−9.75	−10.85	−1.51	−112.27	−1.20
12	0	−1.00	−54.64	−5.67	−22.15	−59	−16.45	−5.50	−6.85	−2.14	−136.12	−0.47
13	−10	−0.44	−74.66	−50.43	−6.28	−28	−8.16	−15.00	−15.85	−2.19	−144.84	−0.79
14	−2	−1.57	−37.87	−0.75	−6.30	−35	−5.44	−7.75	−9.35	−1.04	−178.05	−0.23
15	0	−1.19	−57.27	−12.80	−8.57	−59	−22.43	−2.00	−3.85	−1.92	−149.04	−0.78

Note: The headers g1–g12 represent the constraint functions defined in Equation (16).

It can be observed in Table 1 that, in order to achieve reciprocating stamping, the module of the gear and rack should not be less than 3. When the module is relatively small, the punch blade thickness s_p also decreases accordingly, which is detrimental to the long-term stability and durability of the equipment. Considering that the blade needs to possess a certain level of structural strength, the thickness s_p should be as large as possible. Therefore, the gear module should not be too small and is recommended to be no less than 5. However, as the gear module increases, the stamping stroke as well as the overall dimensions of the punch and die also increase, leading to a reduction in stamping efficiency. Taking the above factors into account, the third, eighth, and tenth sets of data were selected as design schemes for further analysis and comparative study.

4.2. Study on Stamping Motion Based on Co-Simulation with Adams and Simulink

Taking the top-down stamping process as an example, the three design schemes mentioned above were validated through co-simulation using a model built in Adams 2020 and MATLAB/Simulink. Trapezoidal velocity profile planning was employed for motion control of the components. To balance computational cost and simulation efficiency, the acceleration and deceleration time was set to 0.5 s. The maximum rotational speed of the gear was set to 75 r/min, and the maximum linear speed of the reciprocating punch was set to 300 mm/s. Figure 8 shows the block diagram of the model constructed in the Simulink environment. The simulation step size was set to 0.0001 s, with a total simulation duration of 0.8 s.

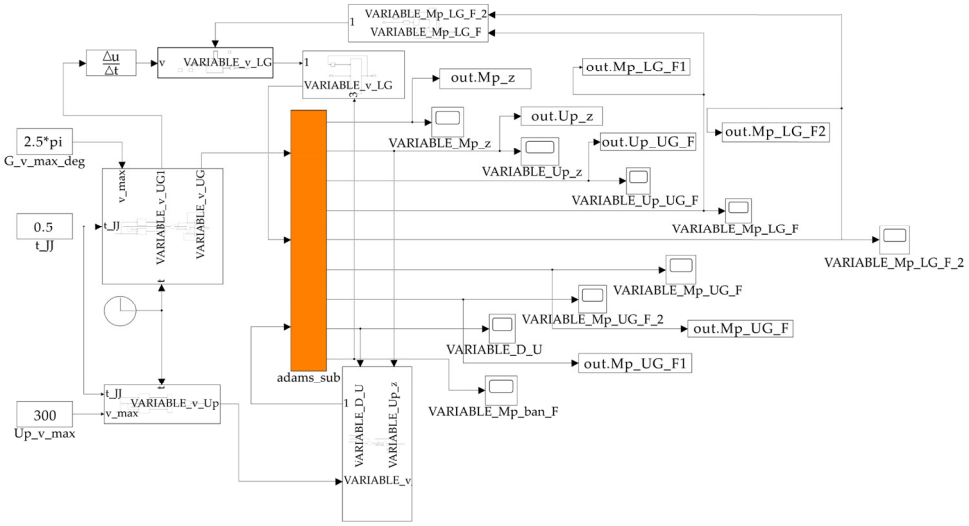


Figure 8. Simulink model block diagram. The orange elements in the figure represent the system setup model in Adams, including the input and output interfaces used for co-simulation with MATLAB/Simulink.

The simulation results are shown in Figures 9–11. Figure 9 displays the displacement and force curves of the reciprocating and single-action punches under Design Scheme 3. As shown in Figure 9a, the reciprocating punch completes the blanking process at 0.5965 s, while the single-action punch finishes the repair operation at 0.6884 s.

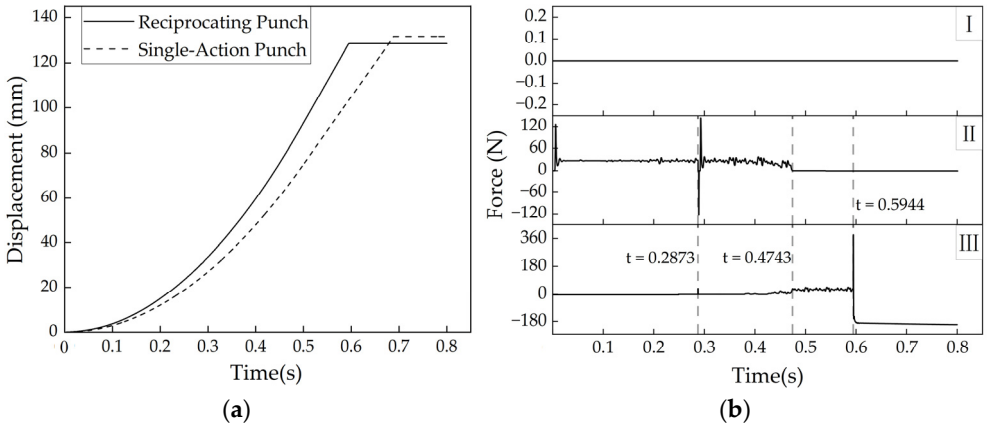


Figure 9. Design Scheme 3: (**a**) displacement curves of punch, (**b**) force curves of punch. Note: Layer I shows the force exerted by the single-action punch on the upper gear; Layer II represents the force from the upper gear on the reciprocating punch; Layer III indicates the force from the lower gear on the reciprocating punch.

In Figure 9b, Layer I shows that the force from the single-action punch on the upper gear remains zero throughout the motion, indicating no interference between its movement and gear rotation, which confirms the rationality of the designed radius r_0. Layer II illustrates that an initial force is applied to the upper gear due to gravity, causing early fluctuations. At 0.2873 s, the reciprocating punch contacts the lower gear, generating a reaction force also seen in Layer III. The forces then stabilize over time. Layer III indicates that the force on the lower gear is more stable than on the upper gear, suggesting that the main dynamic response occurs primarily on the upper gear. At 0.4743 s, the force on the upper gear drops to zero, indicating complete disengagement. From this point onward, the lower gear becomes the primary driver. Its force begins to fluctuate periodically and rises sharply at 0.5944 s, indicating that the punch has reached the bottom of the die and is compacting the waste material.

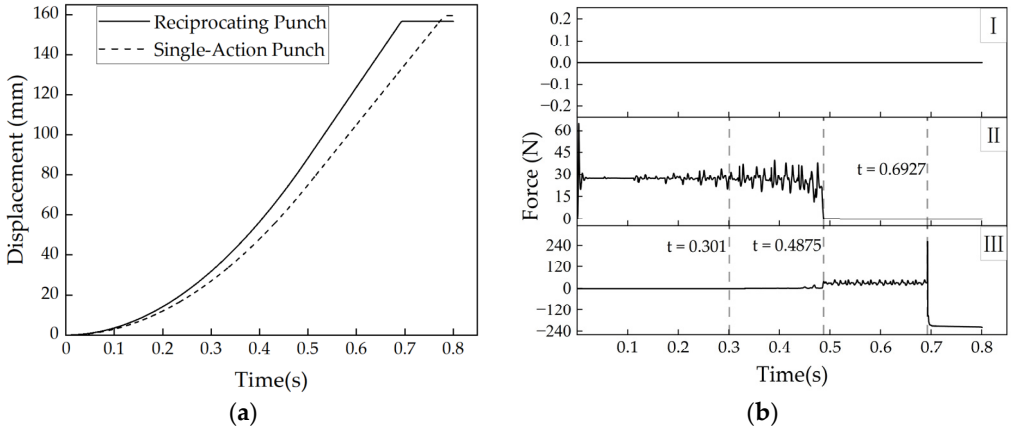


Figure 10. Design Scheme 8: (**a**) displacement curves of punch, (**b**) force curves of punch. Note: Layer I shows the force exerted by the single-action punch on the upper gear; Layer II represents the force from the upper gear on the reciprocating punch; Layer III indicates the force from the lower gear on the reciprocating punch.

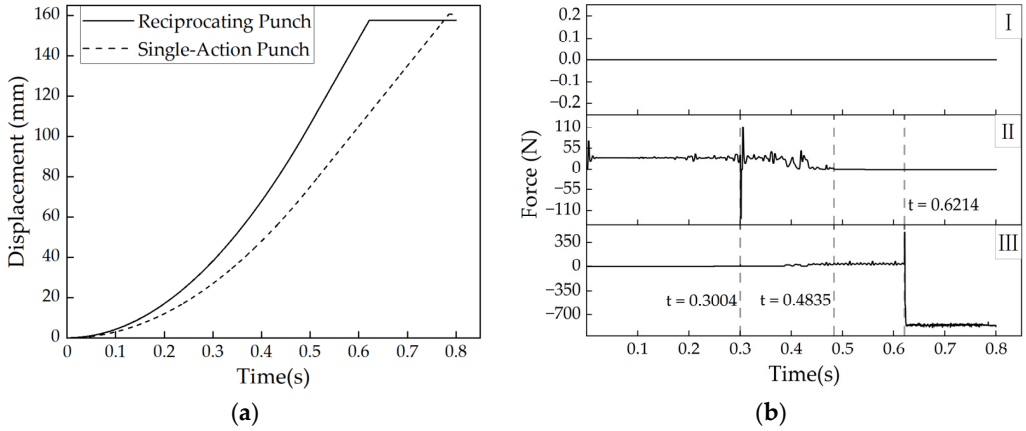


Figure 11. Design Scheme 10: (**a**) displacement curves of punch, (**b**) force curves of punch. Note: Layer I shows the force exerted by the single-action punch on the upper gear; Layer II represents the force from the upper gear on the reciprocating punch; Layer III indicates the force from the lower gear on the reciprocating punch.

Figure 10 shows the displacement and force curves of the reciprocating and single-action punches under Design Scheme 8. In this scheme, the reciprocating punch completes stamping at 0.6976 s, and the single-action punch finishes at 0.7817 s. Compared to Design Scheme 3, the die height increases from 127 to 155, resulting in a longer stamping stroke and an extended overall process time.

As shown in Figure 10b, Layer I indicates that the force from the single-action punch on the upper gear remains zero, confirming no motion interference with the gear system. The reciprocating punch contacts the lower gear at 0.301 s. Unlike in Scheme 3, no sharp force peaks appear in either the upper or lower gears at this stage, indicating smoother synchronized motion and more gradual power transmission. At 0.4875 s, the reciprocating punch disengages from the upper gear and reaches the bottom of the lower die at 0.6927 s. At this point, the punching force rapidly increases, marking the completion of the stamping operation.

Figure 11 shows the displacement and force curves of the reciprocating and single-action punches under Design Scheme 10. The reciprocating punch completes stamping at 0.6251 s. Compared to Design Scheme 8, it has a similar stamping stroke but a shorter operation time, due to a larger gear module and higher linear velocity. The single-action punch finishes at 0.785 s, close to the time in Scheme 8. This suggests that the total system

cycle time is mainly determined by the motion of the single-action punch, highlighting the importance of optimizing its performance. As shown in the force curves, the reciprocating punch contacts the lower gear at 0.3004 s, causing a noticeable force fluctuation on the upper gear. It disengages at 0.4835 s, a value closely aligned with that observed in Scheme 8, and mainly dependent on the reciprocating punch stroke. Finally, the punch reaches the bottom of the die at 0.6214 s.

From the simulation results presented above, it is evident that the constraint analysis and optimization model employed in the stamping process are effective, as all three design schemes successfully complete the stamping task. Among the three, Design Scheme 3 achieves a shorter overall stamping time, which can be attributed to the reduced stroke of the single-action punch. In contrast, the completion times for Design Schemes 8 and 10 increase by approximately 0.1 seconds, leading to a reduction in stamping efficiency of about 14%. Design Scheme 8 exhibits superior motion stability, with smoother gear coordination, which may be influenced by its specific structural parameters and initial positioning. On the other hand, Design Scheme 10 demonstrates no notable advantages in either efficiency or motion stability, resulting in relatively weaker overall performance.

4.3. Veneer Repair Experiment

The veneer repair experimental setup was built based on the geometric structural parameters of Design Scheme 8 (as shown in Figure 12). Design Scheme 8 demonstrated superior stability in the simulation analysis, making it more suitable for the construction of the actual experimental platform.

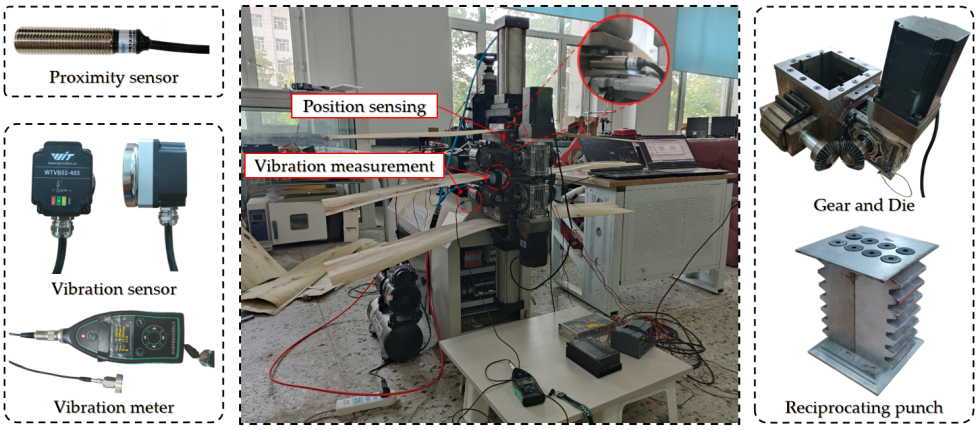


Figure 12. Veneer repair experimental setup.

The experimental setup utilized a stepper gear reducer integrated with bevel gears as the power source. A proximity sensor (OMCH-PR12-2DN, Zhejiang Hugong Automation Technology Co., Ltd., Wenzhou, China) was incorporated into the system to enable feedback control of the reciprocating punch's position state. To evaluate the gear meshing condition during the veneer repair process, magnetic vibration sensors (WTVB02-485, WitMotion Shenzhen Co, Ltd., Shenzhen, China) were mounted on the surfaces of key components, with a sampling interval of 0.115 s, to continuously acquire their vibration response data in real time. Additionally, a vibration meter (AHAI3002, Hangzhou Aihua Intelligent Technology Co., Ltd., Hangzhou, Zhejiang Province, China) was employed as a reference device to assess the timeliness and accuracy of the collected signals.

To accommodate the sampling interval of the vibration sensors and obtain a higher number of sampling points, the rotational speed of the stepper gear reducer was controlled at 45 r/min during the experiment. As shown in Figure 13, the mechanical vibration

response of the reciprocating punch during the repair process is presented. This signal is the most intuitive reflection of the gear meshing state.

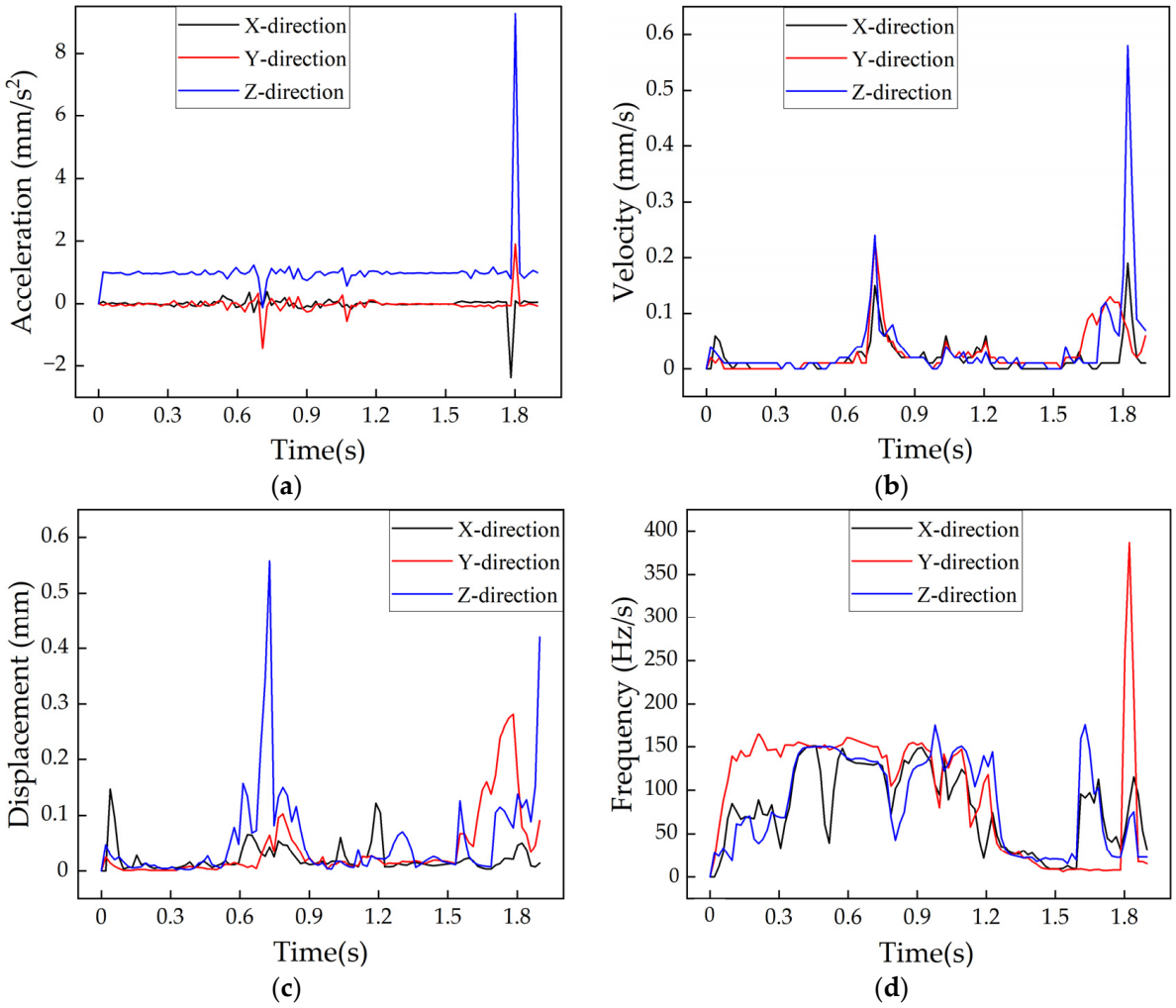
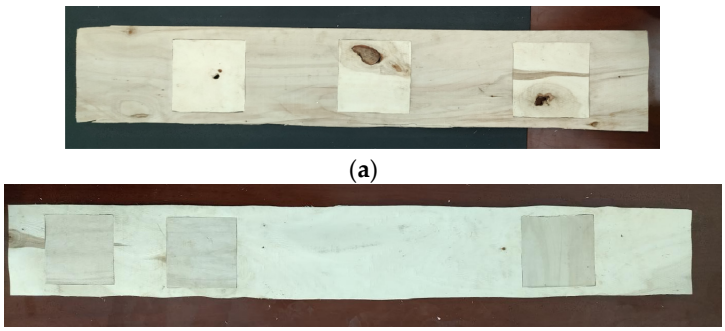


Figure 13. Mechanical vibration during the repair process: (**a**) vibration acceleration, (**b**) vibration velocity, (**c**) vibration displacement, (**d**) vibration frequency.

From the acceleration, velocity, and displacement curves, two distinct peaks can be observed, with the most prominent manifestation occurring along the Z direction. The first peak appears between 0.65 and 0.75 s and corresponds to the contact response of the reciprocating punch with the lower gear. The second peak occurs at the end of the stroke, representing the final impact response. The motion fluctuations during the remaining time intervals are relatively mild. These fluctuations are primarily attributed to manufacturing and installation tolerances in the equipment, as well as the coordinated control between gears. This behavior reflects, to some extent, the complexity of real-world operating conditions.

Despite these minor deviations, the overall trends of the measured curves align well with the theoretical results from the simulation analysis, confirming that the mechanical system is capable of completing the intended task effectively. Furthermore, frequency curve observations indicate that after disengagement, the vibration frequency dominated by the lower gear gradually decays and stabilizes. This phenomenon supports the simulation conclusion that the upper gear plays a dominant role during the coordinated motion.

Figure 14 presents the repair results of the veneer, where the defective areas have been successfully patched, and the waste material is embedded into the holes of the scrap edges. This repair method can effectively improve the utilization rate of the sheet material.



(**a**)

(**b**)

Figure 14. Repair results: (**a**) combination of waste material and patch base blank, (**b**) defective veneer after repair.

5. Conclusions

This paper presents a method for the rapid bidirectional repair of veneer defects, together with an associated device. The device incorporates a punch structure based on rack-and-pinion reciprocating motion. During the repair process, parametric modeling was conducted for both the stamping motion and the geometric structure of the mechanism. By applying rotational transformations within the coordinate system, the geometric relationships of the conjugate tooth profiles under non-standard meshing conditions were derived.

Building upon the parametric model and integrated with multi-objective optimization theory, a constrained optimization model was formulated, with repair efficiency as the primary objective. The NSGA-III algorithm was employed to solve the optimization problem. Subsequently, three optimal parameter sets were selected and utilized in both simulation analysis and experimental platform construction, aiming to validate the feasibility and effectiveness of the proposed method and model. The main findings are summarized as follows:

(1) The experimental platform successfully achieved the removal and repair of defective areas in the veneer, while simultaneously embedding the removed waste material into the holes of the patch substrate to form new composite panels suitable for low-end product manufacturing. This outcome validates the feasibility and effectiveness of the proposed method and model. Moreover, the repair approach significantly improves the utilization rate of sheet materials.

(2) The repair efficiency of the veneer is primarily determined by the stroke of the unidirectional punch. The key to improving efficiency lies in optimizing the motion control of the unidirectional punch and the structural dimensions of the die.

(3) The stamping process of the reciprocating punch from top to bottom can be divided into the following motion stages: upper gear driving alone; engagement with the lower gear; coordinated driving by both upper and lower gears; disengagement of the upper gear; and lower gear driving alone and reaching the end of the stroke. Significant vibration excitation responses occur during the stages of gear engagement and at the end of the stroke, due to the increased contact forces. In contrast, the amplitude fluctuations remain relatively mild throughout the remaining stages. Overall, the vibration induced by the upper gear has a more pronounced effect on the reciprocating punch than that of the lower gear.

This study proposes a feasible technical approach and corresponding mechanical device for repairing defects in veneer sheets. However, the current mathematical model primarily focuses on the geometric constraints between structural dimensions and motion interference, without accounting for the dynamic response during the stamping process or the fatigue life of critical components. Therefore, future research will focus on the development and optimization of mathematical models for system dynamics and component wear life, aiming to further improve the operational stability and long-term durability of the equipment.

Author Contributions: Conceptualization, X.D.; methodology, X.D.; software, X.S. and H.C.; validation, J.L.; formal analysis, C.S.; investigation, J.Y.; resources, J.L.; data curation, X.D.; writing—original draft preparation, C.S.; writing—review and editing, C.S.; supervision, C.Y.; project administration, C.Y.; funding acquisition, C.Y. All authors have read and agreed to the published version of the manuscript.

Funding: This research was supported by the Fundamental Research Funds for the Central Universities (2572023AW61), the Major Scientific and Technological Achievements Transformation Project of Heilongjiang Province (CG23013), and the Heilongjiang Province "double first class" discipline collaborative innovation achievement project (LJGXCG2024-F16).

Institutional Review Board Statement: Not applicable.

Informed Consent Statement: Not applicable.

Data Availability Statement: The data are contained within the article.

Conflicts of Interest: The authors declare no conflicts of interest.

Nomenclature

δ	Blanking clearance
h	Scrap thickness/veneer thickness
s_p	Punch blade thickness
s_a	Tooth tip thickness of the rack gear
P	Pitch point
r_b	Gear base circle radius
m	Module
h_a^*	Addendum coefficient
r	Gear pitch circle radius
r_a	Gear tip circle radius
α_a	Gear tip pressure angle
α'	Meshing angle
α	Pressure angle
z_{R}	Number of rack teeth
a	Center distance
l_{mp}	Reciprocating punch height
s_b	The distance between the upper and lower dies
l_{ud}	Die height
l_{slot}	Slot height
r_0	Cylindrical surface radius of gear
θ	Gear's angular displacement
z_{G}	Actual meshing teeth of gear
t_{slot}	Die thickness

References

1. Ferreira, B.S.; Arroyo, F.N.; Kondo, M.Y.; Santos, H.F.d.; Barreto, R.L.; Dias, A.M.P.G.; Lahr, F.A.R.; Christoforo, A.L.; Campos, C.I.d. Physical and mechanical properties of plywood produced with thermally treated Pinus taeda veneers. *Forests* **2022**, *13*, 1398. [CrossRef]
2. Bekhta, P.; Sedliačik, J.; Jones, D. Effect of short-term thermomechanical densification of wood veneers on the properties of birch plywood. *Eur. J. Wood Wood Prod.* **2018**, *76*, 549–562. [CrossRef]
3. Li, W.; Zhang, Z.; Zhou, G.; Leng, W.; Mei, C. Understanding the interaction between bonding strength and strain distribution of plywood. *Int. J. Adhes. Adhes.* **2020**, *98*, 102506. [CrossRef]
4. Shi, J.; Li, Z.; Zhu, T.; Wang, D.; Ni, C. Defect detection of industry wood veneer based on NAS and multi-channel mask R-CNN. *Sensors* **2020**, *20*, 4398. [CrossRef]
5. Dong, Y.; Ding, A.; Li, Q.; Yuan, L.; Xu, W.; Cui, Z.; Duo, H.; Wang, X. Research on the veneer defect image enhancement algorithm based on AMEF-AGC+. *Sci. Rep.* **2024**, *14*, 26254. [CrossRef]
6. Zhong, L.; Dai, Z.; Zhang, Z.; Sun, Y.; Cao, Y.; Wang, L. Identification and localization of veneer knot defects based on parallel structure fusion approach. *Eur. J. Wood Wood Prod.* **2024**, *82*, 1301–1317. [CrossRef]
7. Hughes, M. Plywood and other veneer-based products. In *Wood Composites*; Elsevier: Amsterdam, The Netherlands, 2015; pp. 69–89. [CrossRef]
8. Cang, S.; Wang, A.-C.; Cao, J. Image restoration on the defects of knots in the veneer based on image decomposition. In Proceedings of the 2010 IEEE International Conference on Intelligent Computing and Intelligent Systems, Xiamen, China, 29–31 October 2010; IEEE: Piscataway, NJ, USA, 2010; pp. 906–910. [CrossRef]
9. Kauranen, E.; Tolonen, E. Veneer Patching Apparatus. U.S. Patent Application No. 13/184,774, 26 January 2012.
10. Patterson, A.; Bertus, B. Method and Device for Repairing Plywood Panel Defects. U.S. Patent Application No. 14/594,951, 23 July 2015.
11. Metz, K. Repair Device, and Method for Repairing a Defect in a Wooden Workpiece. U.S. Patent No. 11,931,916, 19 March 2024.
12. Xie, Y.; Du, L.; Zhao, J.; Liu, C.; Li, W. Multi-objective optimization of process parameters in stamping based on an improved RBM–BPNN network and MOPSO algorithm. *Struct. Multidiscip. Optim.* **2021**, *64*, 4209–4235. [CrossRef]
13. Awasthi, A.; Saxena, K.K.; Arun, V. Sustainable and smart metal forming manufacturing process. *Mater. Today Proc.* **2021**, *44*, 2069–2079. [CrossRef]
14. Kuo, C.-C.; Huang, H.-L.; Li, T.-C.; Fang, K.-L.; Lin, B.-T. Optimization of the pulsating curve for servo stamping of rectangular cup. *J. Manuf. Process.* **2020**, *56*, 990–1000. [CrossRef]
15. Okotete, P.O. Multi-Objective Optimization and Sensitivity Analysis of Forced-Steering Bogies Using Surrogate Models and NSGA-III. Master's Thesis, Carleton University, Ottawa, ON, Canada, 2024.
16. Davoodi, F.; Ashrafizadeh, F.; Atapour, M.; Rikhtehgaran, R. A novel approach for evaluation of load bearing capacity of duplex coatings on aluminum alloy using PLS and SVR models. *Trans. Nonferrous Met. Soc. China* **2022**, *32*, 1834–1851. [CrossRef]
17. Davoodi, F.; Atapour, M.; Ashrafizadeh, F.; Rikhtehgaran, R. Dry sliding wear characteristics of NiP/TiN duplex coated aluminum alloy and wear analysis using response surface method. *J. Mater. Eng. Perform.* **2022**, *31*, 6360–6372. [CrossRef]
18. Zhai, Z.; Kang, X.; Wang, H.; Cui, H.; Li, C.; Mou, Y. Mathematical modeling and multi-objective optimization design of eccentric telescopic rod conveyor. *Struct. Multidiscip. Optim.* **2021**, *63*, 2035–2045. [CrossRef]
19. Ihnát, V.; Lübke, H.; Balberčák, J.; Kuňa, V. Size reduction downcycling of waste wood. Review. *Wood Res* **2020**, *65*, 205–220. [CrossRef]
20. Stanaszek-Tomal, E. Wood-polymer composites as an alternative to the natural environment. In *Proceedings of the IOP Conference Series: Materials Science and Engineering*; IOP: Bristol, UK, 2019; p. 022009. [CrossRef]
21. Härtig, F.; Stein, M. 3D involute gear evaluation–Part I: Workpiece coordinates. *Measurement* **2019**, *134*, 569–573. [CrossRef]
22. Sheng, W.; Li, Z.; Zhang, H.; Zhu, R. Geometry and design of spur gear drive associated with low sliding ratio. *Adv. Mech. Eng.* **2021**, *13*, 16878140211012547. [CrossRef]
23. Mori, K.-i. Review of shearing processes of high strength steel sheets. *J. Manuf. Mater. Process.* **2020**, *4*, 54. [CrossRef]
24. Krobath, M.; Klünsner, T.; Ecker, W.; Deller, M.; Leitner, N.; Marsoner, S. Tensile stresses in fine blanking tools and their relevance to tool fracture behavior. *Int. J. Mach. Tools Manuf.* **2018**, *126*, 44–50. [CrossRef]
25. Aravind, U.; Chakkingal, U.; Venugopal, P. A review of fine blanking: Influence of die design and process parameters on edge quality. *J. Mater. Eng. Perform.* **2021**, *30*, 1–32. [CrossRef]
26. Mori, K.-I.; Abe, Y.; Sedoguchi, K. Delayed fracture in cold blanking of ultra-high strength steel sheets. *CIRP Ann.* **2019**, *68*, 297–300. [CrossRef]
27. Yang, Y.; Liu, C.P. The optimum of clearance for mold in the piercing process with finite element method. *Appl. Mech. Mater.* **2013**, *321*, 324–328. [CrossRef]
28. Reichel, V.; Berlin, W.; Rothe, F.; Beuscher, J.; Dröder, K. Study of shear-cutting mechanisms on wood veneer. *Forests* **2020**, *11*, 703. [CrossRef]

29. Tian, Y.; Guo, Z.; Zhen, W.; Zhao, H. Design and processing of the car models gate blanking die. In Proceedings of the 2016 35th Chinese Control Conference (CCC), Chengdu, China, 27–29 July 2016; pp. 9466–9470. [CrossRef]
30. Wu, W. Design and Analysis of Flat Washer Stamping Compound Mold. In Proceedings of the 2018 8th International Conference on Mechatronics, Computer and Education Informationization (MCEI 2018), Shenyang, China, 18–20 May 2018; Atlantis Press: Dordrecht, The Netherlands, 2018; pp. 386–389. [CrossRef]
31. Xiao, Y.; Yin, K.; Chen, X.; Chen, Z.; Gao, F. Multi-objective optimization design method for the dimensions and control parameters of curling hexapod robot based on application performance. *Mech. Mach. Theory* **2024**, *204*, 105831. [CrossRef]
32. Shi, B.; Zhang, L.; Jiang, Y.; Li, Z.; Xiao, W.; Shang, J.; Chen, X.; Li, M. Three-Phase Transformer Optimization Based on the Multi-Objective Particle Swarm Optimization and Non-Dominated Sorting Genetic Algorithm-3 Hybrid Algorithm. *Energies* **2023**, *16*, 7575. [CrossRef]
33. Liu, X.; Feng, Y.; Zeng, Q.; Hu, X.; Yang, Z. Multi-objective optimization of spraying trajectory planning for large ship blocks using evolutionary computation. *Procedia CIRP* **2021**, *104*, 530–535. [CrossRef]
34. Yong, C.; Kong, X.; Chen, Y.; E, Z.; Cui, K.; Wang, X. Multiobjective scheduling of an active distribution network based on coordinated optimization of source network load. *Appl. Sci.* **2018**, *8*, 1888. [CrossRef]
35. Tian, Y.; Zhu, W.; Zhang, X.; Jin, Y. A practical tutorial on solving optimization problems via PlatEMO. *Neurocomputing* **2023**, *518*, 190–205. [CrossRef]

Disclaimer/Publisher's Note: The statements, opinions and data contained in all publications are solely those of the individual author(s) and contributor(s) and not of MDPI and/or the editor(s). MDPI and/or the editor(s) disclaim responsibility for any injury to people or property resulting from any ideas, methods, instructions or products referred to in the content.